Original Article

Institution of MECHANICAL ENGINEERS
Journal of MECHANICAL ENGINEERING SCIENCE

Proc IMechE Part C:
J Mechanical Engineering Science
0(0) 1–12

DOI: 10.1177/0954406217752746
journals.sagepub.com/home/pic
SAGE

Compensation of vibration-induced pointing error caused by wind disturbances in large antenna

Jie Zhang, Jin Huang, Pengbing Zhao, Wei Liang, Xiaodong Tang and Congsi Wang

Abstract

Under different working conditions, scientists need to ensure that the pointing performance of large reflector antenna; however, wind disturbances are the most tricky problems that minimize the pointing accuracy. This is because the wind disturbances have randomness and time-varying characteristics. Davenport spectrum has been widely used to estimate the frequency domain of wind; moreover, it is also used to design the antenna controller in such a way that the servo angle error caused by wind torque gets minimized significantly. But it is difficult to ensure pointing accuracy without considering the reflector vibration caused by wind force. Therefore, this paper proposes a novel method to overcome wind disturbances. This method introduces the concept of predictable pointing errors in the servo controller. All these predictable errors are induced by vibrations. First, we developed an analysis model to determine pointing errors caused by wind. Second, we develop the wind forecast technique to estimate the future load on antenna structure. Third, using the model predictive control (MPC), we design a novel controller to compensate the future pointing errors. Finally, we conduct a series of tests and analysis. For a 7.3 m antenna, the results indicate that when MPC controller is used in the system, the resultant pointing errors are seven times smaller than the errors witnessed under the traditional controller. This indicates that MPC controller is effective in improving the pointing performance.

Keywords

Reflector antenna, model predictive control, pointing accuracy, reflector vibration, wind disturbances

Date received: 8 September 2017; accepted: 12 December 2017

Introduction

In modern physics and electronics, large antennas have several applications in diverse fields; they are predominantly used in technologies used for detecting gravitational waves, discovering black holes, etc. In order to live up to scientific demands of present day, large antennas are now operated at increasingly higher frequency; therefore, a higher pointing precision is required under such conditions. In China, 110 m Qi Tai telescope (QTT) is the largest antenna building; a pointing accuracy of 1.5 arcs is required in order to operate it at 115 GHz. For the antenna system, it is difficult to maintain a pointing accuracy of 1.5 arcs. This is because many factors have an impact on the pointing accuracy, such as deformation of the antenna dish due to gravity, wind and thermal gradient, dry friction of wheels, etc. All these factors are marred by one major difficulty: the random disturbances in wind.

Through acting on the output of the motor, the pointing performance can be severely disrupted by wind torque.[1] Moreover, scientists have not yet been successful in minimizing the rotation-angle error in the antenna. After analyzing the data representing the frequency spectrum of wind, scientists have conducted several experiments on wind field; these experiments have been widely used to improve the robust ability of servo controller. Because most antennas need high pointing accuracy, we cannot easily implement the proportional-integral-derivative (PID) control strategy; this strategy is most frequently used to achieve satisfactory performance.[2] Wodek Gawronski investigated several modern control techniques, such as linear-quadratic-Gaussian (LQG) control and H∞ control.[3] Compared to PID controllers,

Key Laboratory of Electronic Equipment Structure Design, Ministry of Education, Xidian University, Xi'an, People's Republic of China

Corresponding author:
Jin Huang, Key Laboratory of Electronic Equipment Structure Design, Ministry of Education, Xidian University, Xi'an 710071, Shaanxi, China.
Email: jiezhang1987@xidian.edu.cn

previous studies found that LQG and H∞ controllers are far more efficient in improving the pointing performance; however, a more comprehensive survey must be conducted to validate this finding of previous studies.[4] An active disturbance rejection control method was proposed recently.[5] The experimental results indicate that the capacity of wind disturbance rejection was remarkably ameliorated by this method. However, all of the above control systems only used angle encoder readouts as feedback signal while applying pointing control. The actual performance of controller might not meet the requirement of pointing accuracy regardless of the wind-induced vibration in the structure.

Another main source of pointing errors is the reflector vibration, which is caused by wind force. For a 7.3 m antenna, some experimental results prove that the maximum pointing error is 0.00527°; it is caused by structural deformation when the antenna is subjected to a wind speed of 10 m/s. In comparison, the maximum pointing error that can be measured by a shaft encoder is 0.00768°. When a 10 m antenna is subjected at a wind speed of 10 m/s, the pointing error caused by structure vibration is as large as the encoder error.[6] For a 65 m beam-waveguide antenna, the pointing error caused by vibration accounted for about 32.6% of the total pointing error.[7] For a 110 m antenna, the simulation results reveal that the total pointing error is mainly caused by the reflector vibration.[8]

After thoroughly investigating the above results, we conclude that the pointing errors caused by structure vibration are significant; therefore, they should not be ignored. Moreover, we urgently need to develop a compensation method that effectively reduces the pointing error caused by structure vibration.

To meet the very strict requirement of pointing accuracy, we proposed an active compensation method. With this method, we planned to overcome wind disturbance for large antenna. This paper provides a comprehensive discussion of methods used in this experiment. In The analysis of pointing error caused by wind section, we describe how to build a model that to analyzes the pointing error caused by wind. In The short-term wind forecast model section, we describe how to build a short-term wind forecast model (WFM), which is used to estimate a series of future pointing errors that occur before the disruption of the antenna structure by wind. Thus, it lays a foundation for the compensation in time. In The controller system based on model prediction section 4, we discuss the design of the controller. Our aim is to select a design that effectively grapples with constraint conditions; the optimization problem is transformed into a quadratic programming. In the Analytical example section 5, we comprehensively describe an analytical example. In the Conclusion section, we present all the conclusions with respect to this example.

The analysis of pointing error caused by wind

Wind disturbance is a random phenomenon that exists for a short period of time; therefore, it is difficult to counteract surface vibration by moving each of the segments of the primary surface, which is implemented with hundreds of actuator panels. Interestingly, previous studies proved that these active panels can be used to effectively compensate the pointing error caused by gravity and thermal gradient. In an effort to improve antenna performance under wind load, we need to accurately estimate the pointing error caused by structure vibration. Following estimation, we must immediately compensate the pointing error by altering the rotation angle; therefore, it is absolutely essential to construct a novel analysis model for estimating the pointing error, especially for a large structure with a low natural frequency. This is because such a structure can be easily distorted.

The structural dynamic model

Based on modal coordinate, we constructed a proximate dynamic model of the structure in order to describe the structure distortion. The dynamic model includes two parts: the rigid part is used for determining the rotation angle, whereas the flexible part provides nodal displacements; this model was used for assessing pointing error caused by structural deformation. For an antenna facing wind disturbance, the proximate dynamic model is as follows[9]

$$\begin{bmatrix} J & 0 \\ -\boldsymbol{B_{11}} \cdot J & \boldsymbol{M_m} \end{bmatrix} \begin{bmatrix} \ddot{\theta} \\ \ddot{\boldsymbol{q}}_{\boldsymbol{m}} \end{bmatrix} + \begin{bmatrix} D_r & 0 \\ -\boldsymbol{B_{11}} \cdot D_r & \boldsymbol{D_m} \end{bmatrix} \begin{bmatrix} \dot{\theta} \\ \dot{\boldsymbol{q}}_{\boldsymbol{m}} \end{bmatrix} + \begin{bmatrix} 0 & 0 \\ 0 & \boldsymbol{K_m} \end{bmatrix} \begin{bmatrix} \theta \\ \boldsymbol{q_m} \end{bmatrix} = \begin{bmatrix} T_1 \\ F_s \boldsymbol{B_{12s}} + F_d \boldsymbol{B_{12d}} + F_l \boldsymbol{B_{12l}} \end{bmatrix} \tag{1}$$

$$\boldsymbol{y} = \boldsymbol{C_{mq}} \boldsymbol{q_m} \tag{2}$$

Here J is the moment of inertia; θ is the rotation angle output; T_1 is the sum of motor input and wind torque; D_r is the frictional damping. The diagonal matrices $\boldsymbol{M_m}$, $\boldsymbol{K_m}$, and $\boldsymbol{D_m}$ are the modal mass matrix, modal stiffness matrix, and modal damping matrix, respectively. The inputs of flexible model consist of two parts: torque T_1 and wind force F_s, F_d, F_l. Furthermore, $\boldsymbol{B}_{11}$ is the equivalent modal input matrix induced by the torque T_1. Moreover, $\boldsymbol{B}_{12s}$, $\boldsymbol{B}_{12d}$, $\boldsymbol{B}_{12l}$ are the modal input matrices caused by wind force in different directions, respectively. In addition, $\boldsymbol{C}_{mq}$ is the modal output matrix. Nodal displacement y is obtained from modal displacement $\boldsymbol{q}_m$.

The electromechanical coupled model

Figure 1 presents a schematic diagram of antenna, which has an elevated rotation angle θ_e. The large

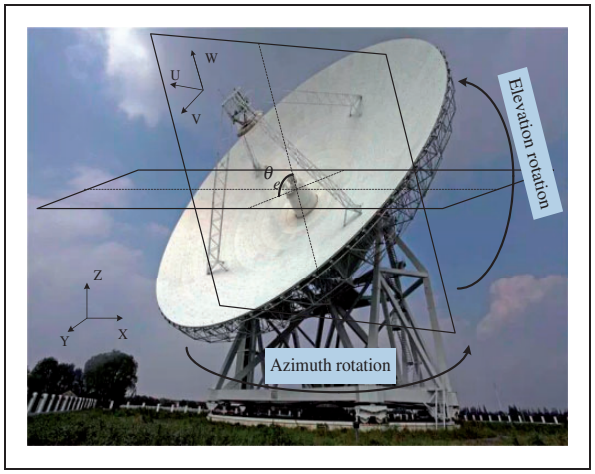

Figure 1. Schematic diagram of the reflector antenna with elevation angle θ_e.

antenna usually rotates with respect to azimuthal and elevation axes. In this analysis, we took into account the orthogonality of rotation directions to estimate the pointing errors accurately in the azimuthal direction.

The total pointing errors consisted of two kinds of errors: the rotation angle error and errors caused by antenna reflector vibration. The rotation angle θ was calculated directly using the proximate dynamic model from (1). The equation for rotation angle error, θ_q, is as follows

$$\theta_q = \theta - \theta_{ref} \tag{3}$$

where θ_{ref} is a reference input.

Reflector deformation also caused pointing errors, which were estimated from node displacements derived from equation (2). For example, consider Cassegrain antenna. The pointing accuracy of this antenna is affected by four main factors: deformation of main reflector, lateral displacement of feed, lateral displacement of sub-reflector, and rotation of sub-reflector.

Figure 2 illustrates the coupling relation of four factors in the aperture plane (i.e. the UW plane shown in Figure 1). Based on the theory of fitting paraboloid,[10] the parameters of the fitting paraboloid were derived after estimating node displacements; these parameters were as follows: i) the vertex moves upwards by an amount d_o; ii) the axis of the fitting paraboloid rotates by ϕ_v; iii) the feed moves by amount d_b; iv) the focal axis of the sub-reflector rotates by θ_s; and v) the lateral sub-reflector moves by amount d_n.

In Figure 2, d_{s1} is the vertical distance between the feed, B', and the focal axis of the sub-reflector; it is then used to calculate a lateral displacement, d_{s2}, of the virtual focus away from the focal axis.

$$d_{s1} = \frac{|-d_b - d_n - \tan\theta_s L_1|}{\sqrt{1+(\tan\theta_s)^2}} = \cos\theta_s |d_b + d_n + \tan\theta_s L_1| \tag{4}$$

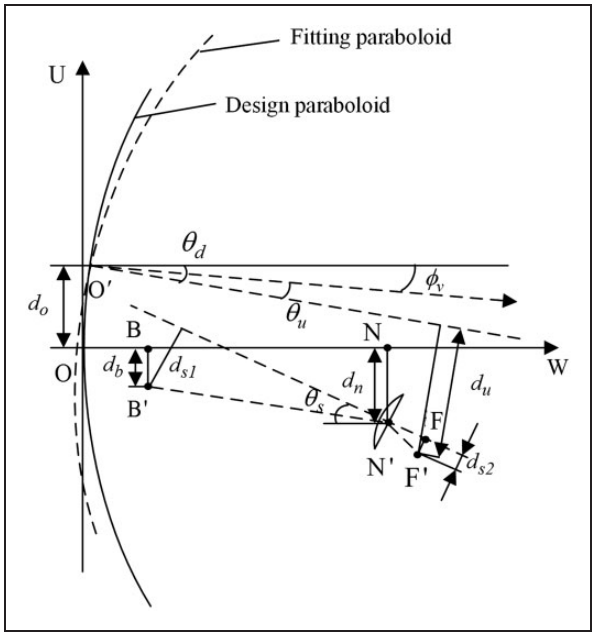

Figure 2. Pointing error caused by deformation of dual reflector antenna.

$$d_{s2} = \frac{d_{s1}}{M} \tag{5}$$

$$M = \frac{L_1}{L_3} \tag{6}$$

Here L_1 is the distance between the feed B and the point N, which is the vertex of the sub-reflector. L_3 is the distance between points N' and F, which is the focus of sub-reflector; M is the scaling factor.

After omitting the vertex displacement of paraboloid along the W-axis, we used equation (7) to calculate the distance, d_u, between the virtual feed and the focal axis of the fitting paraboloid. Furthermore, a pointing deviation θ_u was defined in equation (8) using the distance d_u.

$$d_u = \frac{\left|\begin{array}{l}\tan\phi_v(L_1 + L_3\cos\theta_s - d_{s2}\sin\theta_s) \\ -(d_n + L_3\sin\theta_s + d_{s2}\cos\theta_s) + \tan\phi_v L_2 - d_o\end{array}\right|}{\sqrt{1+(\tan\phi_v)^2}} \tag{7}$$

$$\theta_u = -duK/f \tag{8}$$

Here, L_2 is the distance between points O and B, and f is the focal length. K is the beam deviation factor. The pointing error, θ_d, caused by reflector deformation is expressed as follows

$$\theta_d = \phi_v + \theta_u \tag{9}$$

The short-term wind forecast model

Wind forecast was done using time-domain method, and it was widely used in the field of meteorology and wind power. Some examples of time-series forecast model were discussed, and they were based on the following techniques: Auto-regressive Moving Average (ARMA),[11] fractal interpolation,[12] transfer learning with Deep Neural Networks (DNN),[13] and machine learning ensembles.[14] But they could only be used to calculate the average wind speeds over a large area; these speeds were not accurate enough for estimating the pointing error of antenna under wind load. Light detection and ranging (LIDAR) wind speed measurements was another popular method for forecasting the wind field upstream of a turbine: the instruments used presently provide sufficient ranging capability. Using these instruments, we can perform rapid and accurate radial velocity measurements at a range of locations from a turbine.[15] However, too many Navier–Stokes' equations are needed to estimate the oncoming wind velocity, resulting in low efficiency.

To resolve the problem of smaller spatial and faster temporal dynamics in a typical wind gust and to provide a promising forecast wind velocity, we developed the following WFM: as shown in Figure 3, the several sensors located around the antenna can be used for measuring the speed and direction of wind. The distance between the sample points in a radial direction is 20 m, which is significantly lesser than the characteristic length scales of gust (the boundary of correlation for wind speed). The sampling rate is 100 Hz. The eight sampling points of the wind upstream of antenna (e.g. the eight red triangle sampling points) are used to estimate the oncoming wind at the location away from the antenna (e.g. the green circle sampling point).

The WFM was developed using least square support vector regression (LSSVR).[16] In a given training set $\{(x_i, y_i), x_i \in R^n, y_i \in R, i = 1, \ldots, N\}$

Here x_i is the wind velocity of eight sampling points; and y_i is the wind velocity at the antenna structure located after a few sampling period. Based on these functions and parameters, we constructed the following regression formula

$$f(x) = \boldsymbol{\omega} \cdot \varphi(\boldsymbol{x}) + b \tag{10}$$

The object function of LSSVR can be expressed as follows

$$\text{Min}: \frac{1}{2}\|\boldsymbol{\omega}\|^2 + \frac{1}{2}C\sum_{i=1}^{N}(y_i - f(x_i))^2 \tag{11}$$

$$\text{s.t. } y_i = \boldsymbol{\omega} \cdot \varphi(\boldsymbol{x}) + b + \xi_i \quad \forall\, i = 1, \ldots, N \tag{12}$$

Here C is a regularized parameter that controls the tradeoff between training error minimization and smoothness of an estimated function; $\boldsymbol{\omega}$ is the adjustable weight vector; $\varphi(.)$ maps the input data into a higher dimensional feature space; b is the scalar threshold; and ξ_i is the relaxation factor.

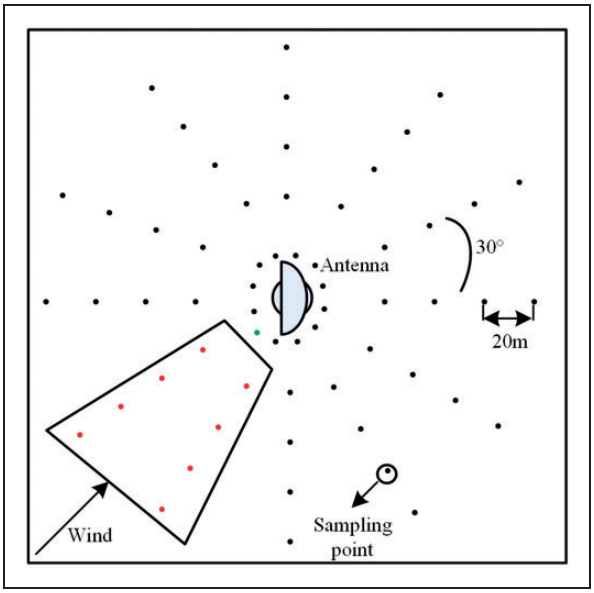

Figure 3. Schematic diagram of wind field test.

After introducing Lagrange function and Lagrange multipliers a_i, we rewrote the solution of the above equation; thus, the solution was as a linear function group

$$\begin{pmatrix} \boldsymbol{\Omega} + \frac{1}{C}\boldsymbol{I} & \boldsymbol{I} \\ \boldsymbol{I}^T & 0 \end{pmatrix}\begin{pmatrix} \boldsymbol{a} \\ b \end{pmatrix} = \begin{pmatrix} \boldsymbol{y} \\ 0 \end{pmatrix} \tag{13}$$

Here $\boldsymbol{I}$ is a unit matrix, $\boldsymbol{a} = \begin{bmatrix} a_1 & a_2 & \ldots & a_N \end{bmatrix}^T$; $\boldsymbol{y} = \begin{bmatrix} y_1 & y_2 & \ldots & y_N \end{bmatrix}^T$; $\boldsymbol{\Omega}_{(i,j)}$ is the element of matrix $\boldsymbol{\Omega}$, and $\boldsymbol{\Omega}_{(i,j)} = \varphi(x_i)^T\varphi(x_j) = k(x_i, x_j)$; $i, j = 1, \ldots, N$.

Note that $\boldsymbol{\omega}$ can be obtained using Lagrange function

$$\boldsymbol{\omega} = \sum_{i=1}^{N} a_i\varphi(x_i) \tag{14}$$

After introducing b and $\boldsymbol{\omega}$ into equation (10), we finally obtained the following regression function

$$f(x) = \sum_{i=1}^{N} a_i\varphi(x_i)\cdot\varphi(\boldsymbol{x}) + b = \sum_{i=1}^{N} a_i k(\boldsymbol{x}, x_i)\cdot + b \tag{15}$$

The forecast wind velocity is derived from regression function. The inputs of the function, x_i, are real-time speeds of eight sampling points. After a few sampling periods, we calculated the forecast wind velocity at the antenna location using equation (15); then,

we used it to estimate pointing errors. During the sampling period, we introduced the test speed into y_i to reconstruct the regression function; it was used to predict wind speed of the next sampling period of the controller.

After estimating the forecast wind velocity, we derived wind force and torque from the following expression of wind pressure q

$$q = \frac{1}{2}\rho v^2 \tag{16}$$

Here ρ is the density of air, and v is wind velocity.

To determine the equivalent wind force on the structure and the equivalent wind torque on the drives, we used the following expressions

$$\text{Resistance force: } F_d = C_d q A \tag{17}$$

$$\text{Lateral force: } F_s = C_s q A \tag{18}$$

$$\text{Lift force: } F_l = C_l q A \tag{19}$$

$$\text{Wind torque: } T = C_M q A D \tag{20}$$

Here C_d, C_s, C_l are wind force coefficients, and C_M is the coefficient of wind torque. These coefficients depend on various factors, such as wind direction, diameter of the antenna, etc. They are obtained from wind tunnel tests.

The controller system based on model prediction

With state estimation and integral control, Figure 4 depicts the model predictive controller (MPC) and it is based on WFM.[17] The antenna pointing model can be treated as a linear system; for the sake of convenience, the multi-input single-output antenna model is decomposed into three single-input single-output models: Model 1 is the servo model in which the input is the motor torque T_m; model 2 is the pointing error model in which the input is the wind torque T_f; and model 3 is the pointing error model in which the input is the wind force F_f.

The state observer

While developing an effective controller, we need to maintain a high accuracy of state estimation as it is a key factor influencing the whole process. To compensate the pointing errors caused by model 2 and model 3, antenna servo motor has to produce a proper torque T_m. With this strategy, we ensure that the state observer is different from other traditional observers. In this case, the state observer would use the final pointing Y_k as a feedback signal and would not be restricted to using only the encoder output θ_1.

Figure 4 illustrates the velocity loop model $(\boldsymbol{A}, \boldsymbol{B}, \boldsymbol{C})$; it includes velocity controller, drivers (motors, gearboxes, and amplifiers), and antenna pointing models. The matrixes of discrete state-space equation, $(\boldsymbol{A_c}, \boldsymbol{B_c}, \boldsymbol{C_c})$, are the controllable and observable expressions of $(\boldsymbol{A}, \boldsymbol{B}, \boldsymbol{C})$[18]; the dynamic property between the two models may be different, but they produce the same effect in the estimation of pointing error. Therefore, the compensation effect can be implemented when the estimation pointing output, $\hat{y}_k$, derived from $(\boldsymbol{A_c}, \boldsymbol{B_c}, \boldsymbol{C_c})$ is same as the actual pointing output, $\boldsymbol{Y_k}$, obtained from $(\boldsymbol{A}, \boldsymbol{B}, \boldsymbol{C})$.

The state estimator is as follows

$$\begin{cases} \hat{\boldsymbol{x}}_{\boldsymbol{k}}(k+1) = \boldsymbol{A_c}\hat{\boldsymbol{x}}_{\boldsymbol{k}}(k) + \boldsymbol{B_c}\boldsymbol{u}(k) + \boldsymbol{Ke}(\boldsymbol{Y_k}(k) - \hat{\boldsymbol{y}}_{\boldsymbol{k}}(k)) \\ \hat{\boldsymbol{y}}_{\boldsymbol{k}}(k+1) = \boldsymbol{C_c}\hat{\boldsymbol{x}}_{\boldsymbol{k}}(k+1) \end{cases} \tag{21}$$

Here $\hat{\boldsymbol{x}}_{\boldsymbol{k}}$ are the estimation states; they are basically assumption states obtained under the condition that the pointing output, $\boldsymbol{Y_k}$, is a rigid rotation angle. Note that $\boldsymbol{Ke}$ is the optimal estimator gain matrix.

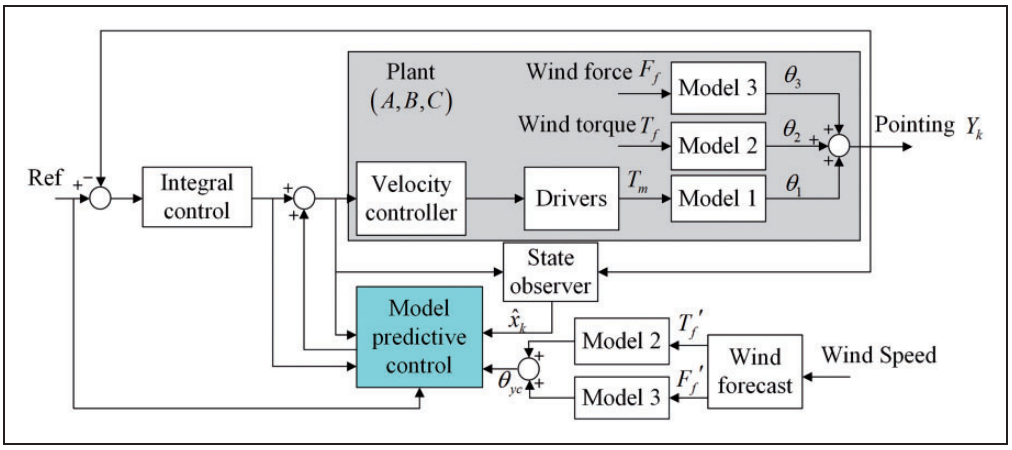

Figure 4. Model predictive controller based on wind forecast model.

$\boldsymbol{Ke}$ can be derived from the equation as follows

$$\boldsymbol{Ke} = \boldsymbol{PeC}_c^T \boldsymbol{R}_e^{-1} \tag{22}$$

where $\boldsymbol{Pe}$ is the unique positive definite solutions of following algebraic equations of the controller

$$\boldsymbol{PeA}_c^T + \boldsymbol{A}_c\boldsymbol{Pe} - \boldsymbol{PeC}_c^T\boldsymbol{R}_e^{-1}\boldsymbol{C}_c\boldsymbol{Pe} + \boldsymbol{Q}_e = \boldsymbol{0} \tag{23}$$

Here $\boldsymbol{Q}_e$ is a positive semi-definite weight matrix, while $\boldsymbol{R}_e$ is a positive scalar.

Model predictive control

By introducing the forecast pointing error caused by the wind, the discrete state-space model of the antenna velocity loop model can be expressed as follows

$$\begin{cases} \boldsymbol{x_k}(k+1) = \boldsymbol{A}_c\boldsymbol{x_k}(k) + \boldsymbol{B}_c\boldsymbol{u}(k) \\ \boldsymbol{Y_k}(k+1) = \boldsymbol{C}_c\boldsymbol{x_k}(k+1) + \boldsymbol{S_k}(k+1) \end{cases} \tag{24}$$

Herein, $\boldsymbol{S_k}$ is the predicted pointing error. The integrator state $\boldsymbol{I_k}$ is chosen as follows

$$\boldsymbol{I_k}(k+1) = \boldsymbol{I_k}(k) + T_s(\boldsymbol{Ref}(k) - \boldsymbol{Y_k}(k)) \tag{25}$$

Herein, T_s is the sampling time. After combining the integrator and the velocity loop model, the augmented system dynamics can be expressed as follows

$$\begin{cases} \bar{\boldsymbol{x}}_{\boldsymbol{k}}(k+1) = \bar{\boldsymbol{A}}_c\bar{\boldsymbol{x}}_{\boldsymbol{k}}(k) + \bar{\boldsymbol{B}}_c\boldsymbol{u}(k) + \boldsymbol{K}\bar{\boldsymbol{R}}\boldsymbol{ef}(k) \\ \boldsymbol{Y_k}(k+1) = \bar{\boldsymbol{C}}_c\bar{\boldsymbol{x}}_{\boldsymbol{k}}(k+1) + \boldsymbol{S_k}(k+1) \end{cases} \tag{26}$$

$$\bar{\boldsymbol{x}}_{\boldsymbol{k}}(k) = \begin{bmatrix} \boldsymbol{x_k}(k) \\ \boldsymbol{I_k}(k) \end{bmatrix} \tag{27}$$

$$\bar{\boldsymbol{A}}_c = \begin{bmatrix} \boldsymbol{A}_c & 0 \\ -\boldsymbol{T_s}\boldsymbol{C}_c & 1 \end{bmatrix} \tag{28}$$

$$\bar{\boldsymbol{B}}_c = \begin{bmatrix} \boldsymbol{B}_c \\ 0 \end{bmatrix} \tag{29}$$

$$\bar{\boldsymbol{K}} = \begin{bmatrix} 0 \\ T_s \end{bmatrix} \bar{\boldsymbol{C}}_c = \begin{bmatrix} \boldsymbol{C}_c & 0 \end{bmatrix} \tag{30}$$

By introducing the integral control dynamics with an integral gain K_i, the input of the velocity loop can be expressed as follows

$$\boldsymbol{u}(k) = \boldsymbol{u}(k-1) + [\,I \quad 0 \quad 0 \quad \cdots]\Delta\hat{\boldsymbol{u}}(k) + \boldsymbol{K_i}\boldsymbol{I_k}(k) \tag{31}$$

$$\Delta\hat{\boldsymbol{u}}(k) = [\,\Delta u(k) \quad \Delta u(k+1) \quad \cdots \quad \Delta u(k+H_p-1)\,]^T \tag{32}$$

Considering the prediction horizon lengths H_p and control horizon H_c, the prediction model can be represented as follows

$$\begin{cases} \boldsymbol{x'_k}(k+1) = \boldsymbol{A'}_c\bar{\boldsymbol{x}}_{\boldsymbol{k}}(k) + \boldsymbol{B'}_c\boldsymbol{u}(k-1) + \boldsymbol{D'}\Delta\hat{\boldsymbol{u}}(k) \\ \qquad\qquad + \boldsymbol{K'Ref'}(k) + \boldsymbol{E'I_k}(k) + \boldsymbol{F'S'_k}(k) \\ \boldsymbol{Y'}_k(k+1) = \boldsymbol{C'}_c\boldsymbol{x'_k}(k+1) + \boldsymbol{S'_k}(k+1) \end{cases} \tag{33}$$

$$\begin{aligned} \boldsymbol{x'_k}(k+1) &= \begin{bmatrix} \bar{\boldsymbol{x}}_{\boldsymbol{k}}(k+1) \\ \bar{\boldsymbol{x}}_{\boldsymbol{k}}(k+2) \\ \cdots \\ \bar{\boldsymbol{x}}_{\boldsymbol{k}}(k+H_p) \end{bmatrix}, \\ \boldsymbol{Y'_k}(k+1) &= \begin{bmatrix} \boldsymbol{Y_k}(k+1) \\ \boldsymbol{Y_k}(k+2) \\ \cdots \\ \boldsymbol{Y_k}(k+H_p) \end{bmatrix} \end{aligned} \tag{34}$$

$$\begin{aligned} \boldsymbol{Ref'}(k) &= \begin{bmatrix} \boldsymbol{Ref}(k) \\ \boldsymbol{Ref}(k+1) \\ \cdots \\ \boldsymbol{Ref}(k+H_p-1) \end{bmatrix}, \\ \boldsymbol{S'_k}(k+1) &= \begin{bmatrix} \boldsymbol{S'_k}(k+1) \\ \boldsymbol{S'_k}(k+2) \\ \cdots \\ \boldsymbol{S'_k}(k+H_p) \end{bmatrix} \end{aligned} \tag{35}$$

$$\boldsymbol{A'}_c = \begin{bmatrix} \bar{\boldsymbol{A}}_c \\ \bar{\boldsymbol{A}}_c^2 + \bar{\boldsymbol{G}}_{c(2,1)}\bar{\boldsymbol{C}}_c\boldsymbol{A'}_{c(1,1)} \\ \cdots \\ \bar{\boldsymbol{A}}_c^{H_p} + \sum_{i=1}^{H_p-1} \bar{\boldsymbol{G}}_{c(H_p,i)}\bar{\boldsymbol{C}}_c\boldsymbol{A'}_{c(i,1)} \end{bmatrix} \tag{36}$$

The subscripts of a matrix (i,j) represent the ith row and the jth column of the fetch from the matrix.

For example, $\bar{\boldsymbol{G}}_{c(2,1)} = \bar{\boldsymbol{G}}_c[\,0 \quad I \quad 0 \quad \ldots \quad 0\,]'$ (37)

$$\boldsymbol{B'}_c = \begin{bmatrix} \bar{\boldsymbol{B}}_c \\ \bar{\boldsymbol{A}}_c\bar{\boldsymbol{B}}_c + \boldsymbol{B}_c + \boldsymbol{G}_{c(2,1)}\bar{\boldsymbol{C}}_c\boldsymbol{B'}_c(1,1) \\ \cdots \\ \sum_{j=0}^{H_p-1} \bar{\boldsymbol{A}}_c^j\bar{\boldsymbol{B}}_c + \sum_{i=1}^{H_p-1} \bar{\boldsymbol{G}}_{c(H_p,i)}\bar{\boldsymbol{C}}_c\boldsymbol{B'}_c(i,1) \end{bmatrix} \tag{38}$$

$$\boldsymbol{C'}_c = \begin{bmatrix} \bar{\boldsymbol{C}}_c & 0 & \ldots & 0 \\ 0 & \bar{\boldsymbol{C}}_c & \ldots & 0 \\ \cdots & \cdots & \cdots & \cdots \\ 0 & 0 & \ldots & \bar{\boldsymbol{C}}_c \end{bmatrix} \tag{39}$$

$$\boldsymbol{D}' = \begin{bmatrix} \bar{\boldsymbol{B}}_c & 0 & \cdots & 0 \\ \bar{\boldsymbol{A}}_c\bar{\boldsymbol{B}}_c + \bar{\boldsymbol{B}}_c + \bar{\boldsymbol{G}}_{c(2,1)}\bar{\boldsymbol{C}}_c\boldsymbol{D}'_{(1,1)} & \bar{\boldsymbol{B}}_c & \cdots & 0 \\ \cdots & \cdots & \cdots & \cdots \\ \sum_{j=0}^{H_p-1} \bar{\boldsymbol{A}}_c^j\bar{\boldsymbol{B}}_c + & & \cdots & \sum_{j=0}^{H_p-H_c} \bar{\boldsymbol{A}}_c^j\bar{\boldsymbol{B}}_c + \\ \sum_{i=1}^{H_p-1} \bar{\boldsymbol{G}}_{c(H_p,i)}\bar{\boldsymbol{C}}_c\boldsymbol{D}'_{(i,1)} & & \cdots & \sum_{i=1}^{H_p-1} \bar{\boldsymbol{G}}_{c(H_p,i)}\bar{\boldsymbol{C}}_c\boldsymbol{D}'_{(i,H_c)} \end{bmatrix} \tag{40}$$

$$\boldsymbol{E}' = \begin{bmatrix} \bar{\boldsymbol{B}}_c K_i \\ \bar{\boldsymbol{A}}_c\bar{\boldsymbol{B}}_c K_i + 2\bar{\boldsymbol{B}}_c K_i + \bar{\boldsymbol{G}}_{c(2,1)}\bar{\boldsymbol{C}}_c\boldsymbol{E}'_{(1,1)} \\ \cdots \\ \sum_{j=1}^{H_p} j\bar{\boldsymbol{A}}_c^{H_p-j}\bar{\boldsymbol{B}}_c K_i + \sum_{i=1}^{H_p-1} \bar{\boldsymbol{G}}_{c(H_p,i)}\bar{\boldsymbol{C}}_c\boldsymbol{E}'_{(i,1)} \end{bmatrix} \tag{41}$$

$$\boldsymbol{K}' = \begin{bmatrix} \bar{\boldsymbol{K}} & 0 & \cdots & 0 \\ \bar{\boldsymbol{A}}_c\bar{\boldsymbol{K}} + \bar{\boldsymbol{B}}_c K_i T_s + \bar{\boldsymbol{G}}_{c(2,1)}\bar{\boldsymbol{C}}_c\boldsymbol{K}'_{(1,1)} & \bar{\boldsymbol{K}} & \cdots & 0 \\ \cdots & \cdots & \cdots & \cdots \\ \bar{\boldsymbol{A}}_c^{H_p-1}\bar{\boldsymbol{K}} + \sum_{j=0}^{H_p-1} j\bar{\boldsymbol{A}}_c^{H_p-j-1}\bar{\boldsymbol{B}}_c K_i T_s + \sum_{i=1}^{H_p-1} \bar{\boldsymbol{G}}_{c(H_p,i)}\bar{\boldsymbol{C}}_c\boldsymbol{K}'_{(i,1)} & & \cdots & \bar{K} + \sum_{i=1}^{H_p-1} \bar{\boldsymbol{G}}_{c(H_p,i)}\bar{\boldsymbol{C}}_c\boldsymbol{D}'_{(i,H_c)} \end{bmatrix} \tag{42}$$

$$\bar{\boldsymbol{G}}_c = \begin{bmatrix} 0 & 0 & \cdots & 0 \\ -\bar{\boldsymbol{B}}_c K_i T_s & 0 & \cdots & 0 \\ \cdots & \cdots & \cdots & \cdots \\ \sum_{j=0}^{H_p-1} -j\bar{\boldsymbol{A}}_c^{H_p-j-1}\bar{\boldsymbol{B}}_c K_i T_s & \cdots & -\bar{\boldsymbol{B}}_c K_i T_s & 0 \end{bmatrix} \tag{43}$$

$$\boldsymbol{F}' = -\boldsymbol{K}' \tag{44}$$

The optimal change of input sequence $\Delta\hat{\boldsymbol{u}}(k)$ is obtained from the appropriately minimized algorithms $J(k)$.

$$J(k) = \frac{1}{2}\left\{ \left\| \boldsymbol{Y}'_{\boldsymbol{k}}(k+1) - \boldsymbol{Ref}'(k+1) \right\|^2 \boldsymbol{Q} + \left\| \Delta\hat{\boldsymbol{u}}(k) \right\|^2 \boldsymbol{R} \right\} \tag{45}$$

The weighting parameters $\boldsymbol{Q}$ and $\boldsymbol{R}$ affected the system output and control input, respectively. Therefore, they certainly satisfied the following conditions: $\boldsymbol{Q} \geqslant 0, \boldsymbol{R} > 0$.

Using quadratic programming, the solution of the question can be transformed to equation (46), and the constraint condition can be expressed as equation (54)

$$\text{Min} : J(k) = \frac{1}{2}\Delta\hat{\boldsymbol{u}}(k)^T \boldsymbol{H}_k \Delta\hat{\boldsymbol{u}}(k) + \Delta\hat{\boldsymbol{u}}(k)^T \boldsymbol{f}_k \tag{46}$$

where

$$\boldsymbol{H}_k = \boldsymbol{D}'\boldsymbol{C}'_c\boldsymbol{Q}\boldsymbol{C}'\boldsymbol{D}' + \boldsymbol{R} \tag{47}$$

$$\boldsymbol{f}_k = \boldsymbol{\sigma}_1\bar{\boldsymbol{x}}_k + \boldsymbol{\sigma}_2\boldsymbol{u}(k-1) + \boldsymbol{\sigma}_3\boldsymbol{I}_k(k) + \boldsymbol{\sigma}_4\boldsymbol{Ref}'(k) + \boldsymbol{\sigma}_5\boldsymbol{S}'_k(k) \tag{48}$$

$$\boldsymbol{\sigma}_1 = \boldsymbol{D}'\boldsymbol{C}'_c\boldsymbol{Q}\boldsymbol{C}_c\boldsymbol{A}'_c \tag{49}$$

$$\boldsymbol{\sigma}_2 = \boldsymbol{D}'\boldsymbol{C}'_c\boldsymbol{Q}\boldsymbol{C}_c\boldsymbol{B}'_c \tag{50}$$

$$\boldsymbol{\sigma}_3 = \boldsymbol{D}'\boldsymbol{C}'_c\boldsymbol{Q}\boldsymbol{C}_c\boldsymbol{E}' \tag{51}$$

$$\boldsymbol{\sigma}_4 = \boldsymbol{D}'\boldsymbol{C}'_c\boldsymbol{Q}\boldsymbol{C}_c\boldsymbol{K}' - \boldsymbol{D}'\boldsymbol{C}'_c\boldsymbol{Q} \tag{52}$$

$$\boldsymbol{\sigma}_5 = -\boldsymbol{D}'\boldsymbol{C}'_c\boldsymbol{Q}\boldsymbol{C}_c\boldsymbol{F}' \tag{53}$$

$$\begin{bmatrix} u_{\min} \\ u_{\min} \\ \cdots \\ u_{\min} \\ Y_{\min} \\ Y_{\min} \\ \cdots \\ Y_{\min} \end{bmatrix} \leqslant \begin{bmatrix} \boldsymbol{u}(k) \\ \boldsymbol{u}(k+1) \\ \cdots \\ \boldsymbol{u}(k+H_c-1) \\ \boldsymbol{Y}(k) \\ \boldsymbol{Y}(k+1) \\ \cdots \\ \boldsymbol{Y}(k+H_p-1) \end{bmatrix} \leqslant \begin{bmatrix} u_{\max} \\ u_{\max} \\ \cdots \\ u_{\max} \\ Y_{\max} \\ Y_{\max} \\ \cdots \\ Y_{\max} \end{bmatrix} \tag{54}$$

Analytical example

To simulate the antenna in the wind, we constructed the wind field and antenna structure using computational fluid dynamics software. As shown in Figure 5, some equivalent obstacles are used to simulate complex terrain. With this strategy, we increase the turbulence characteristics of the wind field. The wind direction is mostly inclined along the X-axis. Figure 6 shows the input (wind gust) in time series; the gust is estimated from Davenport wind spectrum.

By performing transient analysis, we obtained the wind speed of sampling points. We estimated the predictive wind speed using LSSVR. As shown in Figure 7, we compared the test speed with the prediction speed when the forecasting time span was 0.15 s

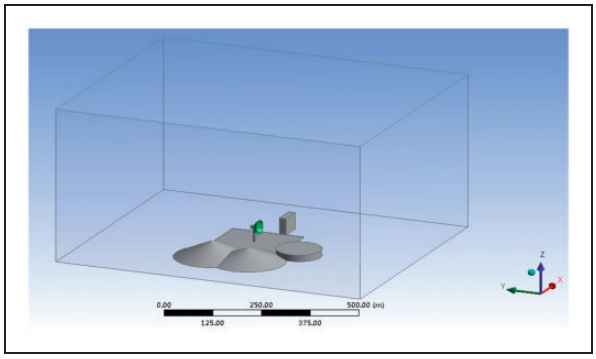

Figure 5. Simulation of the antenna in wind field.

(The sampling time of the servo system is 0.05 s.). The test speed is calculated using the computational fluid dynamics software. In addition, the predictive speed was derived from WFM. We found that the maximum prediction error is about 0.3116 m/s. Therefore, an accurate predictive wind speed, identical to the test results, is suitable for engineering applications.

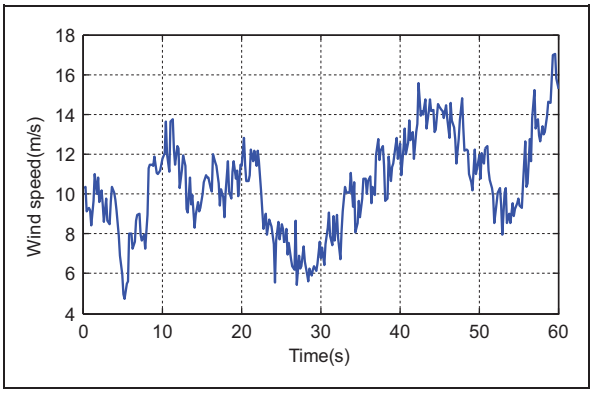

Figure 6. The input wind gust.

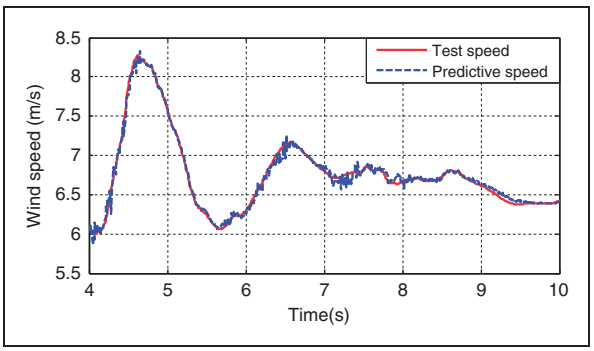

Figure 7. The comparison between test speed and the prediction speed.

Consider the case of a 7.3m Ka-band antenna: the finite element model and the real structure are shown in Figure 8. To verify the correctness of this dynamic model, we performed the load deformation test. Then, the data of test results was presented in Table 1. The results indicate that the maximum node displacement of the finite element model is almost same as that of the actual antenna. Therefore, the dynamic model can be used for obtaining the analytical model.

As shown in Figure 9, when using a traditional PID controller, under the wind speed of 10 m/s, after the initial stage, the maximum rigid pointing error (RPE) is 0.00768°, which is a rotation angle error caused by wind torque and could be measured by encoder, and it is an important object of attention in the traditional control method. The maximum flexible pointing error (FRE) is 0.00408° which is caused by wind-induced flexible oscillation of the reflective surface, and it is of the same order of magnitude as the RPE, so the FRE could not be ignored. As a consequence, the total maximum pointing error (TPE) would be 0.0103°, and it is the actual pointing error of the electromagnetic propagation.

Table 1. Load deformation test results.

Load (kg)	Maximum test result (mm)	Maximum calculation result (mm)	Relative error (%)
100	−1.236	−1.163	5.91
50	−0.506	−0.582	15.01

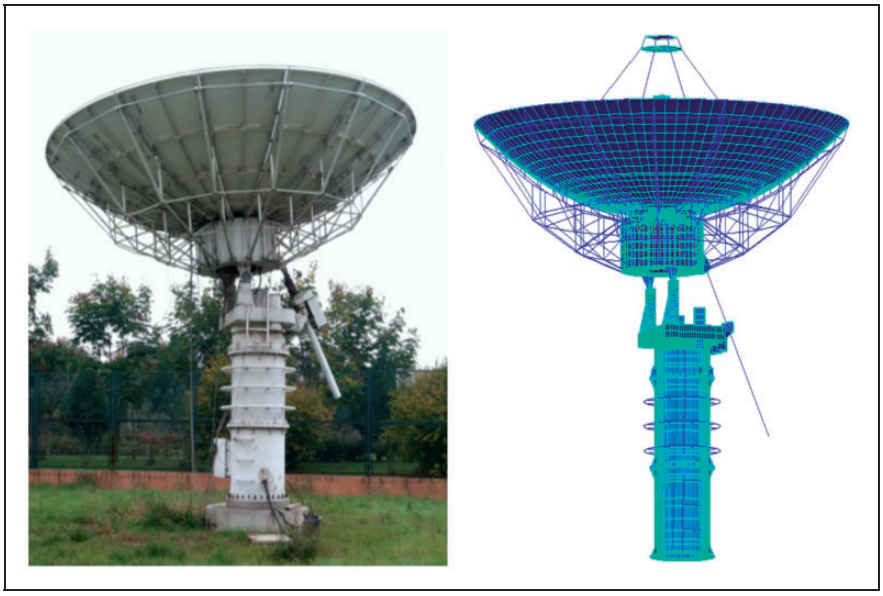

Figure 8. The actual 7.3 m antenna and the finite element model.

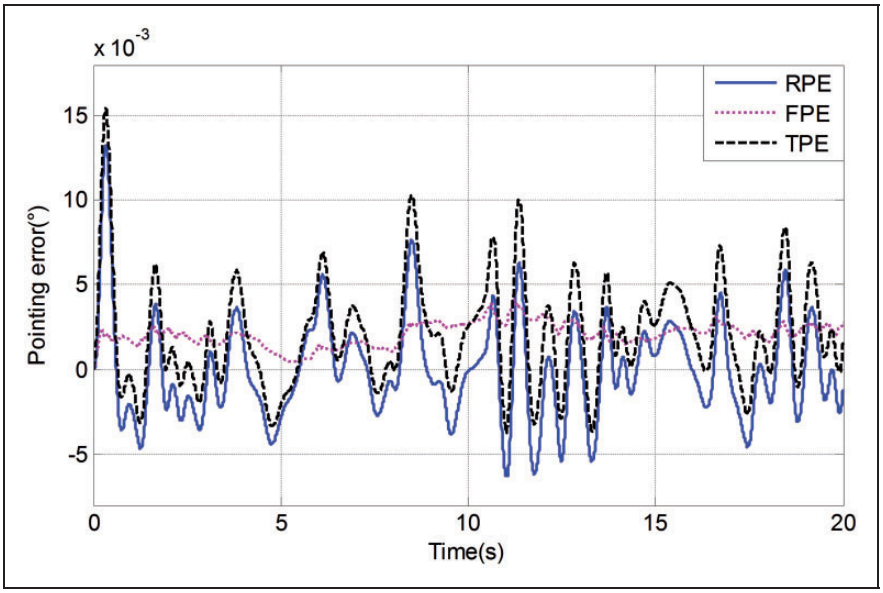

Figure 9. Antenna pointing error under wind-load.

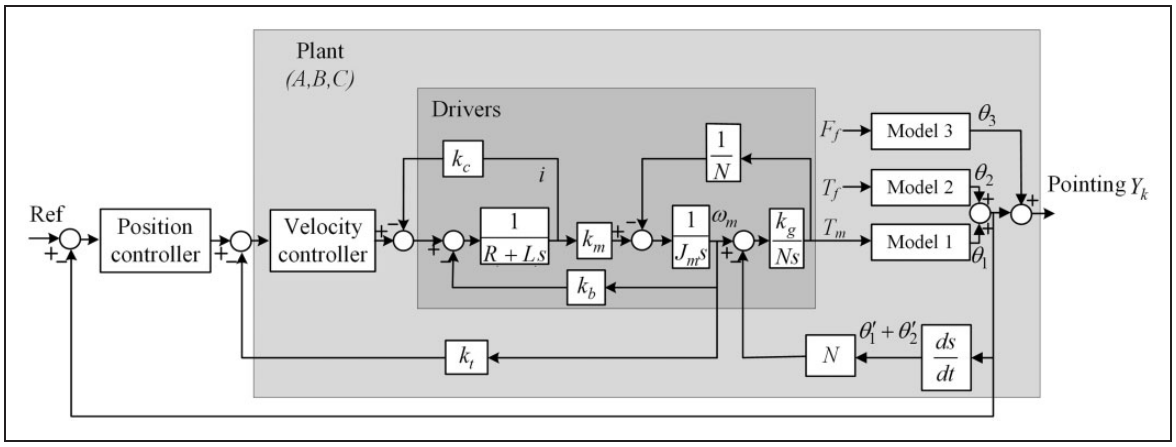

Figure 10. The traditional servo control system with PID controller.

Table 2. System parameters.

Symbol	Quantity	Value
R_a (Ω)	Motor resistance	0.52
L_a (H)	Motor inductance	0.007
k_b (V s/rad)	Armature constant	0.3
k_m (Nm/A)	Motor torque constant	0.89
k_c (V /A)	Current feedback coefficient	0.85
k_t (V s/rad)	Velocity feedback coefficient	0.08
J_m (Nm/s^2)	The inertia of the motor and the brake	0.02
k_g (Nm/rad)	The stiffness of the reducer	1.68×10^7
N(–)	The reducer gear ratio	420

Table 3. Simulation parameters.

Parameters	Value
Elevation angle θ_e (°)	45
Average wind speed v_m (m/s)	10
Wind direction ϕ (°)	70
Sampling time(s)	0.05
Simulation time (s)	20

To verify the correctness of the analysis of the pointing error caused by wind, we compared the error obtained from this experiment's pointing error model with the error simulated using electromagnetic simulation software (GRASP). The relative error is only about 1.86%. The results indicate that our proposed analysis model shows a decent performance when it is used to estimate the pointing error caused by wind.

Figure 10 illustrates the traditional servo control system with PID controller (T-PID). Table 2 presents the parameters of the system architecture. Furthermore, Table 3 presents the simulation parameters. The PID control system (FR-PID) was based on

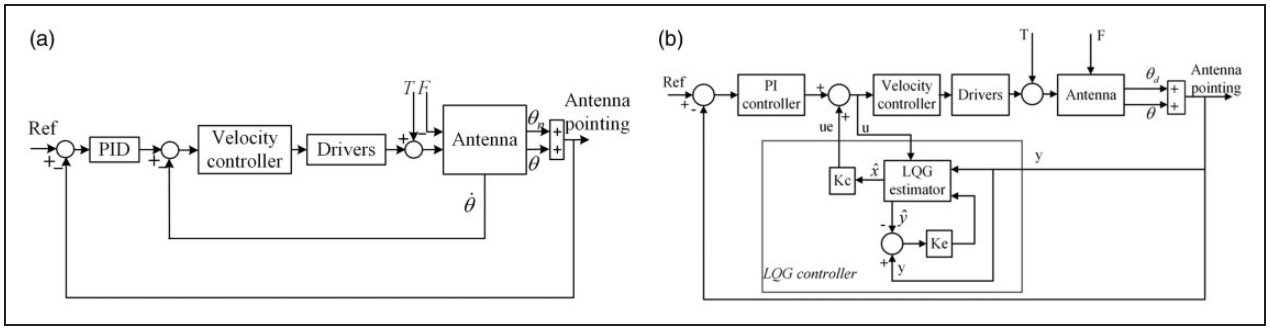

Figure 11. Traditional control system based on the flexible-rigid hybrid (FRH) model.

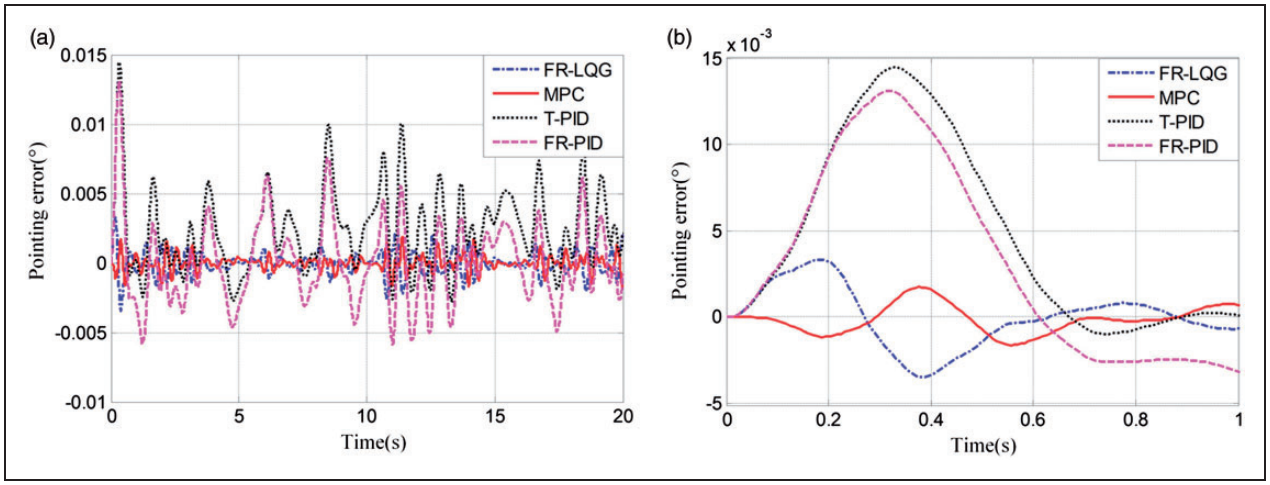

Figure 12. Pointing performance with different control methods.

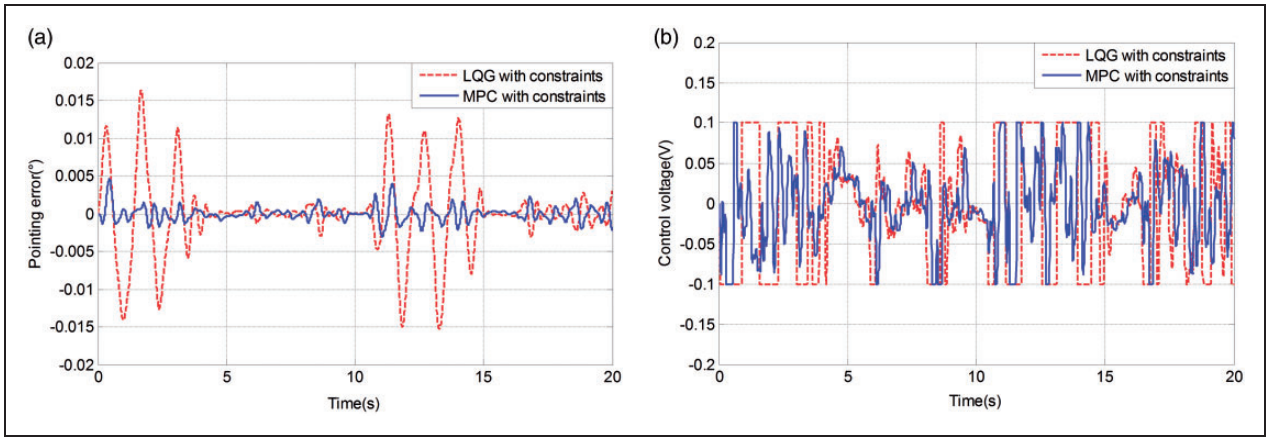

Figure 13. Comparison between the different control methods with constraints.

a flexible-rigid hybrid model (i.e. the analysis model proposed in this paper); it contained the feedback signal that included both rigid error and flexible pointing error, as shown in Figure 11(a). Furthermore, the LQG controller for flexible antenna is based on a flexible-rigid hybrid model described in a previous study[18]; it is depicted vividly in Figure 11(b).

Figure 12(a) illustrates how the pointing performances of the antenna servo system vary with the use of different control methods. The maximum errors in T-PID, FR-PID, and FR-LQG are 0.0103°, 0.0074°, and 0.0024°, respectively. However, it is only 0.0018° when MPC is used in the system. The root mean square (RMS) error is 0.0042° and 0.0031° with T-PID and FR-PID, respectively; however,

the RMS error decreases sharply to 0.0008° with FR-LQG. Furthermore, it dips down to only 0.0006° with the use of MPC. Under an MPC controller, the pointing errors are significantly smaller than the errors arising from the T-PID controller (5.72 times smaller than the maximum error and seven times smaller than RMS error).

The MPC controller has features that are completely different from those of the FR-LQG controller. The MPC controller is designed in such a way that it can effectively compensate the future pointing errors caused by wind. The biggest advantage of this controller is that it effectively reduces the pointing error in the initial stage, which is in favor of restriction for effect of paroxysmal fitful wind. Figure 12(b) provides a comparison of the different compensation effects in the initial stage. The maximum pointing error is only about 0.0017° with MPC, so it is almost half of that with FR-LQG. In this experiment, the proposed controller has good suppressing effects on wind that is both paroxysmal and fitful; such kind of wind outperforms the FR-LQG controller.

The advantages of constrain handling from the use of MPC was analyzed, under the considering constraints (the input voltage of the position loop is required between −0.1 V and 0.1 V as shown in Figure 13(b)), the pointing performance with the MPC controller significantly outperforms the performance with LQG controller as shown in Figure 13(a). The max pointing error with LQG is bigger than 0.015°, and the max pointing error with MPC is less than 0.005°.

Conclusion

When there is a continuous increase in the diameter of a large antenna, we carefully evaluate the vibrations caused by a wind-induced reflector. This is because such vibrations cause remarkable pointing errors and performance degradation. To improve the pointing accuracy of the antenna, we developed an analytical model. This model estimates the pointing errors induced by vibration. Furthermore, we also successfully developed a model predictive control that was actually based on the wind forecasting model. Thereafter, an optimal control action was derived from the quadratic programming problem. The simulation results indicate that the proposed method significantly outperforms traditional methods.

The main outcomes can be summarized as follows.

1. This wind forecast model for estimating the wind speed in short term which could be used to estimate the future pointing error is proposed for the first time.
2. Using the model predictive control (MPC), by introducing the predictable pointing errors, we design a controller to compensate the future pointing errors caused by wind.

Declaration of Conflicting Interests

The author(s) declared no potential conflicts of interest with respect to the research, authorship, and/or publication of this article.

Funding

The author(s) disclosed receipt of the following financial support for the research, authorship, and/or publication of this article: This work was supported by grants received under various program: the National 973 Program under (Grant No. 2015CB857100), the National Natural Science Foundation of China under (Grant No. 51705387 and 51575419), the China Postdoctoral Science Foundation under (Grant No. 2017M613078), the National 111 Project under (Grant No. B14042), and the Fundamental Research Funds for the Central Universities under (Grant No. XJS17069).

References

1. Gawronski W. Three models of wind-gust disturbances for the analysis of antenna pointing accuracy. Caltech. JPL, Pasedena, CA. Technical Report, 2002, pp.42–149.
2. Gawronski W and Souccar K. Control systems of the large millimeter telescope. *IEEE Antennas Propagat Magazine* 2005; 47: 41–49.
3. Gawronski W. Antenna control systems: from PI to H infinity. *IEEE Antennas Propagat Magazine* 2001; 43: 52–60.
4. Gawronski W. Control and pointing challenges of large antennas and telescopes. *IEEE Transact Control Syst Technol* 2007; 15: 276–289.
5. Qiu D, Sun M, Wang Z, et al. Practical wind-disturbance rejection for large deep space observatory antenna. *IEEE Transact Control Syst Technol* 2014; 22: 1983–1990.
6. Ukita N. Wind-induced pointing errors and surface deformation of a 10-m sub-millimeter antenna. In: *Conference on ground-based and airborne telescopes*, San Diego, CA, 28 July 2010, pp.77331D1–77331D11.
7. Zhang J, Huang J, Wang S, et al. An active pointing compensator for large beam waveguide antenna under wind disturbance. *IEEE/ASME Transact Mechatron* 2015; 21: 860–871.
8. Zhang J, Huang J, Song R, et al. Analysis of reflector vibration-induced pointing errors for large antennas subject to wind disturbance. *IEEE Antennas Propagat Magazine* 2015; 57: 46–61.
9. Zhang J, Huang J, Zhou J, et al. A compensator for large antennas based on pointing error estimation under a wind load. *IEEE Transact Control Syst Technol* 2017; 25: 95–134.
10. Duan BY and Wang CS. Reflector antenna distortion analysis using MEFCM. *IEEE Transact Antennas Propagat* 2009; 57: 3409–3413.
11. Ergin E and Jing S. ARMA based approaches for forecasting the tuple of wind speed and direction. *Appl Energy* 2011; 88: 1405–1414.
12. Xiu C, Wang T, Tian M, et al. Short-term prediction method of wind speed series based on fractal interpolation. *Chaos, Solitons Fractal* 2014; 68: 89–97.

13. Hu Q, Zhang R and Zhou Y. Transfer learning for short-term wind speed prediction with deep neural networks. *Renew Energy* 2016; 85: 83–95.
14. Heinermann J and Kramer O. Machine learning ensembles for wind power prediction. *Renew Energy* 2016; 89: 671–679.
15. Towers P and Jones BL. Real-time wind field re-construction from LiDAR measurements using a dynamic wind model and state estimation. *Wind Energy* 2016; 19: 133–150.
16. Goethals I, Pelchmans K, Suykens JAK, et al. Subspace identification of Hammerstein systems using least squares support vector machines. *IEEE Transact Automat Control* 2005; 50: 1509–1519.
17. Lin C-Y and Liu Y-C. Precision tracking control and constraint handling of mechatronic servo systems using model predictive control. *IEEE/ASME Transact Mechatron* 2012; 17: 593–605.
18. Gawronski W. *Modeling and control of antennas and telescopes*. New York, NY: Springer, 2004, pp.95–134.